

Article

Experimental Investigation on Permeability Evolution of Dolomite Caprock under Triaxial Compression

Deng Xu ¹ , Jianfeng Liu ^{1,2,*}, Zhide Wu ², Lu Wang ¹, Hejuan Liu ³, Fukun Xiao ⁴, Yin Zeng ¹ and Cheng Lyu ¹

¹ State Key Laboratory of Hydraulic and Mountain River Engineering, Sichuan University, Chengdu 610065, China; xudeng@stu.scu.edu.cn (D.X.); 1220170051@mail.xhu.edu.cn (L.W.); zengyin@hbsi.edu.cn (Y.Z.); lvchengaust@163.com (C.L.)

² CNPC Key Laboratory of Oil and Gas Underground Storage Engineering, Langfang 065007, China; wuzhide69@petrochina.com.cn

³ State Key Experiments in Geotechnical Mechanics and Engineering, Chinese Academy of Sciences, Institute of Rock and Soil Mechanics, Wuhan 430071, China; hjliu@whrsm.ac.cn

⁴ Heilongjiang Ground Pressure & Gas Control in Deep Mining Key Laboratory, Heilongjiang University of Science and Technology, Harbin 150022, China; xiaofukun@hotmail.com

* Correspondence: liujf@scu.edu.cn

Received: 15 October 2020; Accepted: 2 December 2020; Published: 11 December 2020



Abstract: In order to study the influence of different confining pressures on the stability and airtightness of dolomite underground gas storage, a permeability test under hydrostatic confining pressure, conventional triaxial compression test and gas–solid coupling test under triaxial compression were carried out on MTS815 test machine. During the tests, an acoustic emission (AE) monitoring system was also employed to estimate the rock damage. The experimental results showed that the relationships between permeability, porosity and hydrostatic confining pressure were exponential function and power function, respectively. Increasing confining pressure reduced the porosity and permeability of dolomite, and increased its triaxial compressive strength, but the addition of nitrogen reduced the compressive strength of dolomite by 10~30%, the higher the confining pressure, the smaller the difference. Compared with the maximum permeability under 15 MPa, confining pressure in the gas–solid coupling experiment, the maximum permeability under confining pressure of 30, 45, and 60 MPa is reduced by 42.0%, 84.4%, and 97.9%, respectively. In addition, the AE activity of dolomite decreases significantly with the increase in confining pressure, which also delayed the arrival of the AE active period.

Keywords: dolomite; confining pressure effect; permeability characteristics; acoustic emission

1. Introduction

In order to reserve energy resources, many countries choose to build underground storage [1–3]. Many international scholars have started theoretical research on the construction of salt cavern gas storage in the 1960s and 1970s [4,5]. The construction of underground gas storage in China started relatively late. There are 25 underground gas storage stations distributed all over the country to provide dispatching work for peak natural gas consumption [6]. Many gas storages in the world are built in salt caverns, and the surrounding rocks and caprocks are salt rock minerals with stable mechanical properties and high purity. Moreover, the geological distribution of salt mound is relatively simple. The surrounding rock is of high-purity salt rock. The lithology of caprock is mainly salt-bearing rock, such as anhydrite [7], argillaceous salt rock, dolomite, limestone [8], etc. In the process of construction of underground energy and gas storage in China, different caprocks and lithology will inevitably

lead to different tightness of underground gas storage. The proven caprock lithology of underground gas storage in China mainly includes salt rock [9], gypsum rock [10], dolomite [11], limestone [12], mudstone [13], etc. These typical caprock rocks can be basically divided into soft rock, represented by salt rock, and hard brittle rock, represented by dolomite.

In view of the particularity of caprock in underground gas storage, many international scholars have studied the mechanical properties of caprock from experimental and theoretical perspectives, and obtained some achievements. As early as 1979, Tillerson [14] discussed the creep law of salt rock and analyzed the long-term stability of underground gas storage in salt caverns by means of conventional creep test and numerical simulation. In 1984, Hansen et al. [15] carried out a quasi-static triaxial compression test and rock facies study of natural salt rock in different areas, pointed out the mechanical characteristic parameters of each kind of salt rock, and evaluated the physical deformation state of natural salt rock. Based on the extended Drucker Prager law, Hunsche et al. [16,17] studied the relationship between peak strength and residual strength, confining pressure and loading path during the failure process of salt rock under true triaxial compression. Ni Xinfeng [18] analyzed the diagenetic characteristics and the main controlling factors of airtightness of Cambrian subsalt dolomite reservoir in central Tarim Basin. Based on in situ core sampling and thin section micro-analysis, Shao L. [19] focused on the petrological and reservoir characteristics of dolomite reservoir in Tarim Basin. The study on the geomechanical genesis of dolomite reservoir by two Chinese scholars greatly enriched the research results of dolomite caprock in oil and gas storages in this area.

The effectiveness of caprock in underground gas storage involves not only stress and deformation, but also gas tightness. Permeability is an important parameter which can reflect whether the gas tightness is good or not. De Las Cuevas [20] studied the relationship between porosity and permeability characteristics of salt rock by means of meso observation and from the perspective of pore characteristics. Colin J. Peach [21] obtained the influence characteristics of brittle plastic deformation on permeability of salt rock according to the permeability test during the loading process of synthetic salt rock. Benjamin Michael Tutolo [22] analyzed the seepage path in a CO₂ sealed reservoir according to the permeability change in dolomite reservoir. According to the evolution characteristics of acoustic emission in the process of rock seepage, Jiang Changbao [23] analyzed the relationship between coal seepage characteristics, acoustic emission characteristics and energy dissipation based on the seepage evolution in the process of coal cyclic load failure. Similarly, Guo [24] analyzed the permeability change law and acoustic emission evolution characteristics during the coal-loading failure process according to the permeability test experiment of coal samples under cyclic loading. S. D. Butt [25] studied the permeability characteristics and AE characteristics of easily outburst sandstone in underground coal mine of Nova Scotia, Canada, based on the rock permeability equipment and acoustic emission monitoring device that were independently developed.

Although the research on the cap rock of underground gas storage has achieved initial results, most of them are soft rock such as salt rock, and the research on hard brittle caprock such as dolomite is not enough. As typical carbonate caprock of gas reservoir, dolomite is supposed to have excellent characteristics such as a compact structure, low permeability, good gas sealing capacity, etc. Therefore, it is necessary to study the mechanical properties and permeability characteristics of dolomite caprock, so as to explore its stability and airtightness as an underground gas storage caprock. In this paper, the permeability test under hydrostatic confining pressure, conventional triaxial test and gas–solid coupling test under triaxial compression were carried out for a dolomite gas storage in Xinjiang, China. The influence of confining pressure on the mechanical properties, acoustic emission characteristics and permeability characteristics of dolomite under different test conditions was studied.

2. Experiments

2.1. Specimen Preparation

The dolomite used in those tests was taken from one gas storage of China, and all specimens were from the same rock block, whose depth was about 1200 m. According to the standard of engineering rock mass test method [26], the dry turning lathe method was adopted to process the specimen with a diameter of 38 mm and a height of 76 mm, as shown in Figure 1. The rock powder of this batch of specimens was tested by X-ray diffractometer. The X-ray diffraction (XRD) analysis results of the dolomite are shown in Figure 2. The mineral composition of the dolomite was 90% dolomite, 5% quartz, 2% calcite, 2% feldspar and 1% clay minerals.



Figure 1. Dolomite specimens.

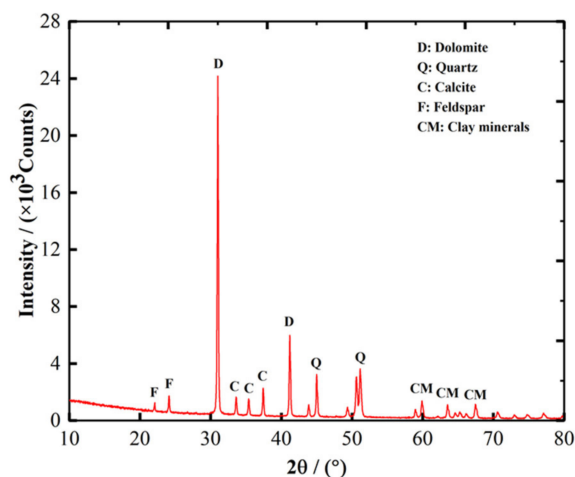


Figure 2. X-ray diffraction analysis results of dolomite.

2.2. Testing Apparatus and Methods

The test was divided into three parts. In the first part, in order to obtain the variation rules of gas permeability and porosity parameters with confining pressure, AP-608 overburden permeameter was used to test the permeability of two dolomite specimens, whose basic parameters are shown in Table 1, under different hydrostatic confining pressures. Figure 3 shows the test equipment and schematic diagram. The equipment consists of a computer data acquisition system, gas seepage system and hydrostatic confining pressure loading system. The maximum confining pressure can be loaded to 65 MPa, the permeability measurement range is 0.0001~10 mD ($1 \text{ mD} = 0.982 \times 10^{-15} \text{ m}^2$), and the minimum porosity can be measured to 0.1%. Stable nitrogen was used as seepage medium in this test.

Table 1. Dolomite specimens in this part ($1 \text{ mD} = 0.982 \times 10^{-15} \text{ m}^2$).

Specimen Number	Diameter D/mm	Height H/mm	Mass m/g	Density $\rho/\text{g}\cdot\text{cm}^{-3}$	Initial Porosity $\omega/\%$	Initial Permeability K/mD
d-1	37.91	75.92	233.01	2.72	4.22	1.54
d-2	38.09	76.01	232.75	2.69	4.67	1.98

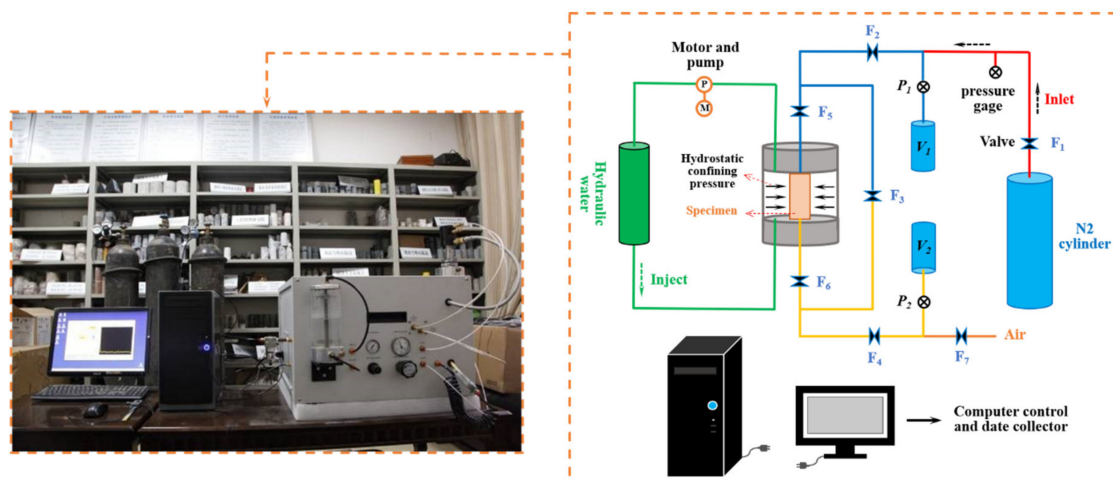


Figure 3. AP-608 overburden permeameter and its principle.

The transient gas pulse attenuation method [27] was used in the test, and the principle is shown in Figure 3. During the test, open valves F1~F6, close F7, inject nitrogen into the upper and lower ends of the specimen to ensure that the air pressure at both ends of the specimen is constant at P_0 . Then close valves F1 and F3, and slowly open and close F7 valve repeatedly to reduce the air pressure at the lower end of the specimen to form a stable initial pressure difference ΔP . Under the action of gas pressure difference, the gas pressure at the upper end decreases and the pressure at the lower end rises, until the air pressure at both ends reaches a new equilibrium state. According to the attenuation formula of gas in the rock specimen and the parameters of the specimen itself, the permeability calculation formula under this method can be obtained

$$k = \ln\left(\frac{\Delta P_0}{\Delta P_t} \frac{\mu \eta L}{A t}\right) / \left(\frac{1}{V_1} + \frac{1}{V_2}\right) \quad (1)$$

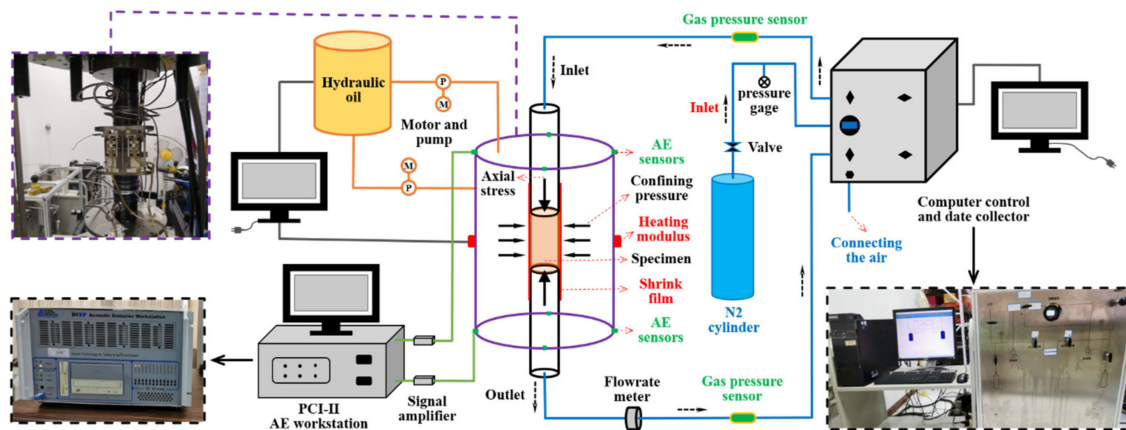
where ΔP_0 is the initial pressure difference between the two ends of the sample (MPa), t is the duration of one penetration test (s), ΔP_t is the pressure difference between the two ends of the specimen at t (MPa), μ is the dynamic viscosity coefficient of nitrogen in the permeation medium (Pa·s), η is the gas compressibility of nitrogen (Pa^{-1}), L is the height of the specimen (m), A is the cross-sectional area of the specimen (m^2), V_1 and V_2 refer to the volume of upper and lower gas pressure buffer bottles (m^3).

Put the specimen into the equipment at room temperature, input the relevant parameters of the specimen and the target value of hydrostatic confining pressure. After the equipment completes the sealing self-inspection, the permeability and porosity of the specimen under the hydrostatic confining pressure can be tested. The hydrostatic confining pressure values of this test are 5, 10, 15, 25, 35, 45, 55 MPa, respectively.

The second part and the third part were the conventional triaxial test and gas–solid coupling test of dolomite. The specimen parameters of these two parts are given in Table 2. These two tests were carried out on the improved MTS815 rock mechanics testing system. The gas permeability equipment developed by ourselves was added to the original system, which can carry out the gas–solid coupling test. At the same time, the system can monitor acoustic emission in real time. Figure 4 shows the working diagram, its main operation parameters include the maximum axial pressure of 4600 kN and the maximum confining pressure of 140 MPa, In addition, the ranges of axial extensometer and circumferential extensometer of are -5 ± 5 mm and -2.5 ± 8 mm, and its test accuracy is 0.5% RO.

Table 2. Dolomite specimens in this part.

Test	Specimen Number	σ_3/MPa	D/mm	H/mm	m/g	$\rho/\text{g}\cdot\text{cm}^{-3}$	$\omega/\%$	K/mD
Conventional triaxial	d-3	15	38.00	76.05	233.30	2.71	4.20	1.53
	d-4	45	37.92	75.89	234.64	2.74	3.99	1.43
	d-5	60	38.13	76.17	234.74	2.70	4.15	1.51
Gas–solid coupling	d-6	15	38.15	76.12	238.27	2.74	4.17	1.52
	d-7	30	38.09	76.16	239.80	2.76	4.09	1.48
	d-8	45	37.98	75.94	237.49	2.76	4.05	1.46
	d-9	60	38.11	76.08	238.21	2.74	4.12	1.50

**Figure 4.** Improved MTS815 rock mechanics testing system.

According to the above test methods, the test steps are as follows, in which the penetration test in steps 3 and 5 was not carried out on the specimens of d-3, d-4 and d-5:

1. The dolomite specimen was completely wrapped with shrink film and placed on the test platform. Then, we installed the axial extensometer and circumferential extensometer, closed the triaxial pressure chamber and installed the acoustic emission sensors outside. At last, the acoustic emission instrument was adjusted to the best condition;
2. Filled the triaxial pressure chamber with hydraulic oil and applied the confining pressure to the target value (σ_3 in Table 2). The confining pressure loading rate was set at 3 MPa/min;
3. After the confining pressure loading was completed, nitrogen was injected into both ends of the sample by gas permeation equipment to stabilize the pressure difference between the upper and lower ends at 3 MPa. Then, a permeability test was conducted, and the permeability was taken as the initial permeability before axial loading;
4. The axial loading was controlled by force and circumferential displacement, successively. Firstly, the specimen was loaded to the yield stress point at the rate of 30 kN/min, and then loaded to the residual stress stage at the circumferential displacement rate of 0.02 mm/min;
5. During the axial loading process, permeability tests were carried out at different strain points, and at least 12 penetration tests were conducted during the whole loading process, including no fewer than eight times before the peak value, one time at the peak stress point and no fewer than three times after the peak value.

3. Experiment Results and Discussion

3.1. Permeability and Porosity under Hydrostatic Confining Pressure

Figure 5 shows the relationship between permeability, porosity and hydrostatic confining pressure of dolomite specimens. Taking d-1 specimen as an example, under the confining pressures of 5, 10, 15, 25, 35, 45 and 55 MPa, the porosity is 3.618%, 2.965%, 2.602%, 2.182%, 1.769%, 1.527% and 1.256%, respectively, and the permeability is 0.7951, 0.2455, 0.0985, 0.0674, 0.0092, 0.0045 and 0.0024 mD (1 mD = $0.982 \times 10^{-15} \text{ m}^2$), respectively. When the hydrostatic confining pressure increases from 5 to 10 MPa, the porosity and permeability of dolomite specimens decrease by 18.1% and 69.1%, respectively. The confining pressure has a great binding effect on permeability, due to the deformation of the crystalline grain skeleton in dolomite under the influence of confining pressure. As a result, the microfracture channels in the bedding development position are closed, and the gas permeability channels are blocked and isolated, which greatly reduce the permeability.

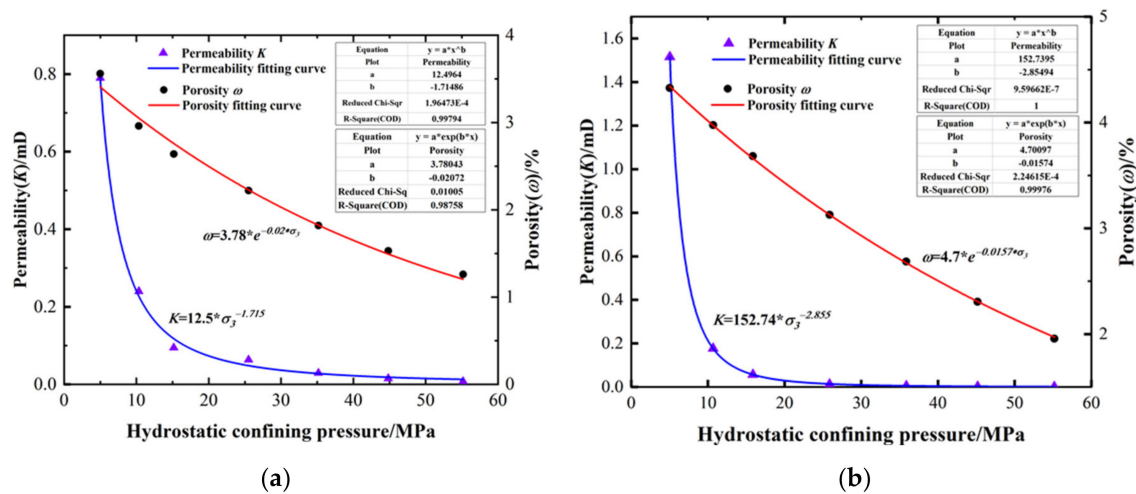


Figure 5. Permeability and porosity versus hydrostatic confining pressure. (a) Sample d-1; (b) Sample d-2. (1 mD = $0.982 \times 10^{-15} \text{ m}^2$).

The fitting curves of permeability, porosity and hydrostatic confining pressure in Figure 5 show that the relationship between permeability and hydrostatic confining pressure is exponential function, and that between porosity and hydrostatic confining pressure is power function, which can be expressed by Formulas (2) and (3)

$$k = A * P^B \tag{2}$$

$$\omega = a * e^{b*P} \tag{3}$$

where k is the permeability (mD), ω is the porosity (%), P is the hydrostatic confining pressure (MPa), A, B, a, b are constants. The curve-fitting effect was good, and all of the correlation coefficient R^2 was above 0.98.

3.2. Confining Pressure Effects on Mechanical Properties of Dolomite

Figure 6 shows the stress–strain curves of dolomite under different confining pressures. When the confining pressure is less than 60 MPa, the stress–strain curve presents a brittle deformation failure state, which is manifested as the stress dropping sharply after the peak stress point, while maintaining a certain amount of residual stress. However, under the confining pressure of 60 MPa, the stress is still stable after reaching the peak value, and there is no stress drop phenomenon, showing a ductile deformation state. With the increase in confining pressure, the peak stress, residual stress and strain at the peak stress point increase synchronously. Taking Figure 6b as an example, when the confining

pressure increases from 30 to 60 MPa, the peak stress increases by 12.4%, which indicates that the confining pressure strengthens the compressive strength of dolomite. After comparing the strength of dolomite under the two test schemes, we find that the peak stress of conventional triaxial specimen is 10~30% higher than that of gas–solid coupling specimen under the same confining pressure, and the residual stress is also the same, which indicates that the compressive strength of dolomite is weakened by nitrogen.

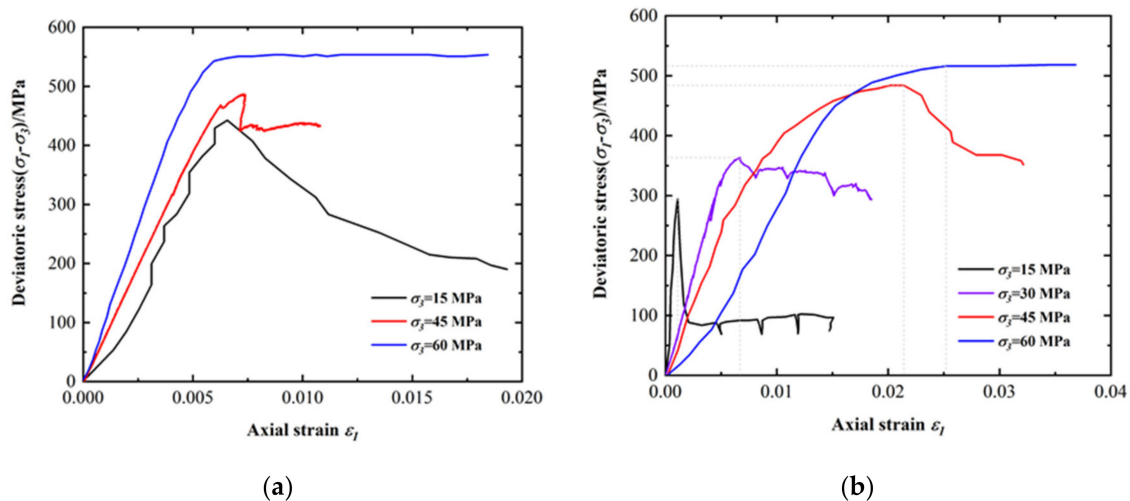


Figure 6. Stress–strain curves of dolomite under different confining pressures. (a) Conventional triaxial compression; (b) Triaxial compression under gas solid coupling.

Furthermore, after analyzing the slopes of the ascending sections of each curve in Figure 6, it is found that with the increase in confining pressure, the slope in Figure 6a increases gradually, while that in Figure 6b decreases gradually. The reason is that the axial deformation of specimen is mainly affected by confining pressure under conventional triaxial condition. With the increase in confining pressure, the axial deformation of specimen under unit axial pressure decreases, resulting in the increase in curve slope. However, in the case of gas–solid coupling, under the same axial pressure, the larger the confining pressure is, the greater the deformation of the sample, which shows that the slope of the curve decreases.

Dolomite is a crystalline mineral [28], the internal crystal size is relatively uniform, but at the same time, there are micro-bedding fissures [29]. Figure 7 shows the failure state of dolomite specimens under gas–solid coupling. Under external stress, the internal crystalline grain skeleton is deformed, and the deformation accumulates continuously, leading to the fracture of the specimen. Under the confining pressures of 15 and 30 MPa, the shear failure occurs in the specimen and the macro crack surface is formed, moreover, there are small cracks around the macro crack. The dolomite specimens under 45 MPa confining pressure do not have large cracks, but there are many short cracks at its ends. This is due to the joint action of strong compaction and high confining pressure at the end of the specimen. However, under the confining pressure of 60 MPa, no macroscopic cracks are found, but the end of the specimen is slightly expanded.

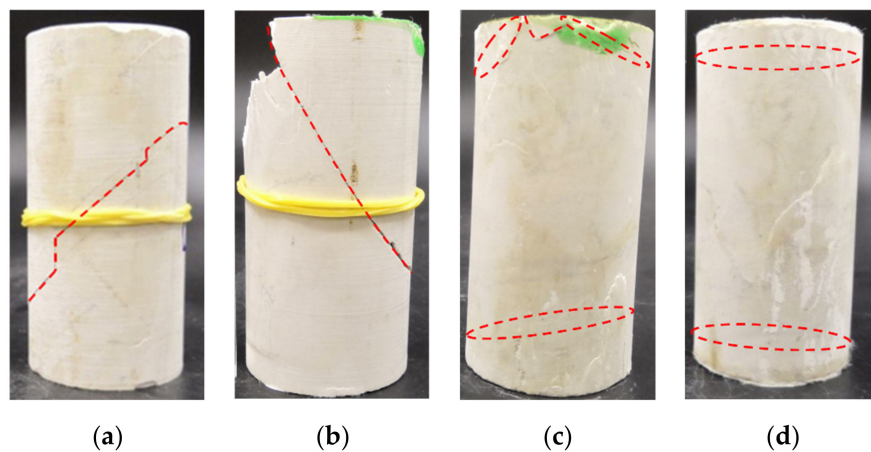


Figure 7. State of dolomite specimens after failure under gas solid coupling. (a) $\sigma_3 = 15$ MPa; (b) $\sigma_3 = 30$ MPa; (c) $\sigma_3 = 45$ MPa; (d) $\sigma_3 = 60$ MPa.

3.3. Confining Pressure Effects on Permeability under Gas Solid Coupling

Figure 8 shows the evolution of dolomite permeability with strain under different confining pressures. The permeability of dolomite is kept within $2.83 \times 10^{-18} \text{ m}^2$ to $3.96 \times 10^{-15} \text{ m}^2$ in the whole test process. The initial permeability decreases with the increase in confining pressure. The increase in confining pressure has a binding effect on the permeability of dolomite, which is consistent with the permeability change rule under hydrostatic confining pressure. In addition, with the increase in confining pressure, the variation range of permeability in the whole loading process decreases gradually.

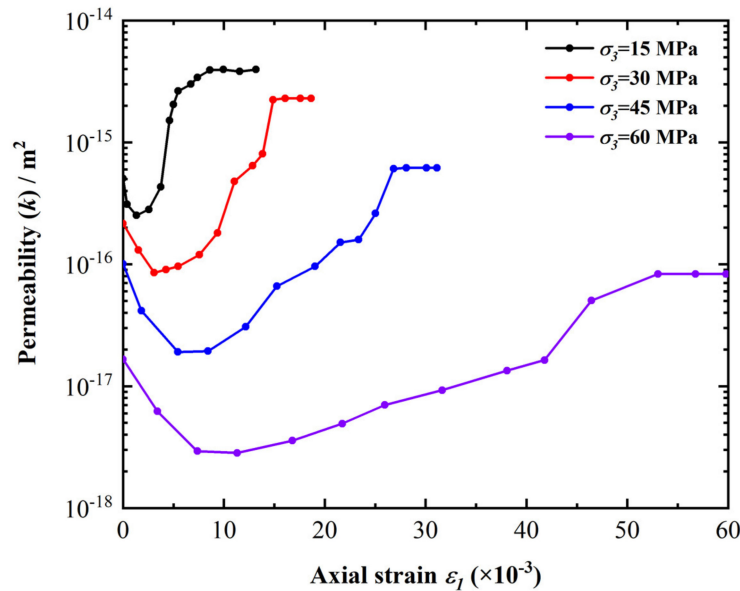


Figure 8. Permeability evolution of dolomite under different confining pressures.

Under the same confining pressure, with the increase in axial load, the permeability–strain curves show a trend of ‘first decrease, then increase, and last tend to be stable’. Taking Figure 9a as an example, under the confining pressure of 15 MPa, the decrease in permeability in the initial loading stage is mainly due to the fact that the internal microcracks of dolomite are continuously compacted by axial stress, the permeability channels gradually decrease and the tortuosity increases, so the permeability decreases rapidly. With the increase in axial stress, the specimens enter the stage of microfracture development. These fractures promote the seepage of nitrogen, so the permeability gradually increases.

When the peak stress is reached, the internal fractures of the specimen are fully developed, and then a macro through permeability channel is formed. Therefore, the gas permeability is more active, and the permeability increases sharply. When it comes to the residual deformation stage, the increasing rate of permeability gradually decreases, and the final permeability tends to the same level and reaches the peak value.

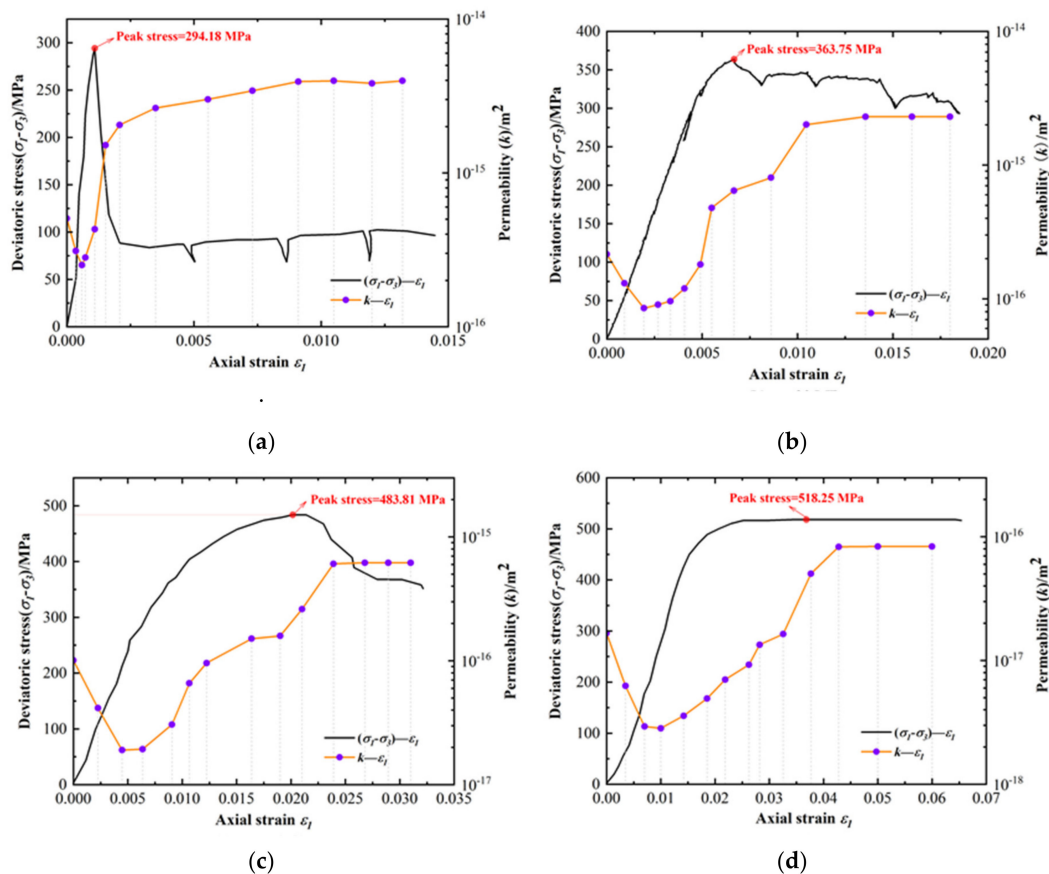


Figure 9. Stress-strain-permeability curves of dolomite during loading. (a) $\sigma_3 = 15$ MPa; (b) $\sigma_3 = 30$ MPa; (c) $\sigma_3 = 45$ MPa; (d) $\sigma_3 = 60$ MPa.

Combined with the failure state of the specimens in Figure 7, the macro fracture surface of the specimens under 15 and 30 MPa confining pressure is formed, forming a stable gas permeability channel, so the final permeability does not change. However, the specimens under 45 and 60 MPa confining pressures do not form macroscopic fracture surface, and the permeability remains unchanged at the later stage of loading, which is due to the ‘damage-compensation’ characteristics of dolomite under a high confining pressure. Under axial stress compression, the intact particles in dolomite will be destroyed and new cracks will be formed. The natural damaged particles will aggravate the damage and form micro-mineral crystals. Under the continuous action of a high confining pressure, these micro-mineral crystals will be gradually squeezed and filled into the new cracks, which hinders the penetration of the permeability channel. The ‘damage-compensation’ cycle between axial pressure and confining pressure is formed in dolomite, so the permeability will not change in the later stage of loading even if the macro-fracture surface is not produced.

3.4. Confining Pressure Effects on Acoustic Emission Characteristics under Gas Solid Coupling

Figure 10 shows the AE evolution characteristics of dolomite specimens under the low confining pressure of 15 MPa and high confining pressure of 45 MPa. Through comparative analysis, it can be found that, under the condition of low confining pressure, the acoustic emission energy rate and ring

count rate of dolomite have a long “quiet period”, and its duration accounts for three-fifths of the entire test process. It is because of this that dolomite is a typical hard brittle rock, and crystal mineral particles have a strong ability to absorb energy, thus delaying the arrival of active acoustic emission period, the active period of AE is mainly distributed near the peak stress. However, under a high confining pressure, the active period of AE is mainly distributed in the residual deformation stage after the peak stress, which indicates that the increase in confining pressure further delays the arrival of AE active period.

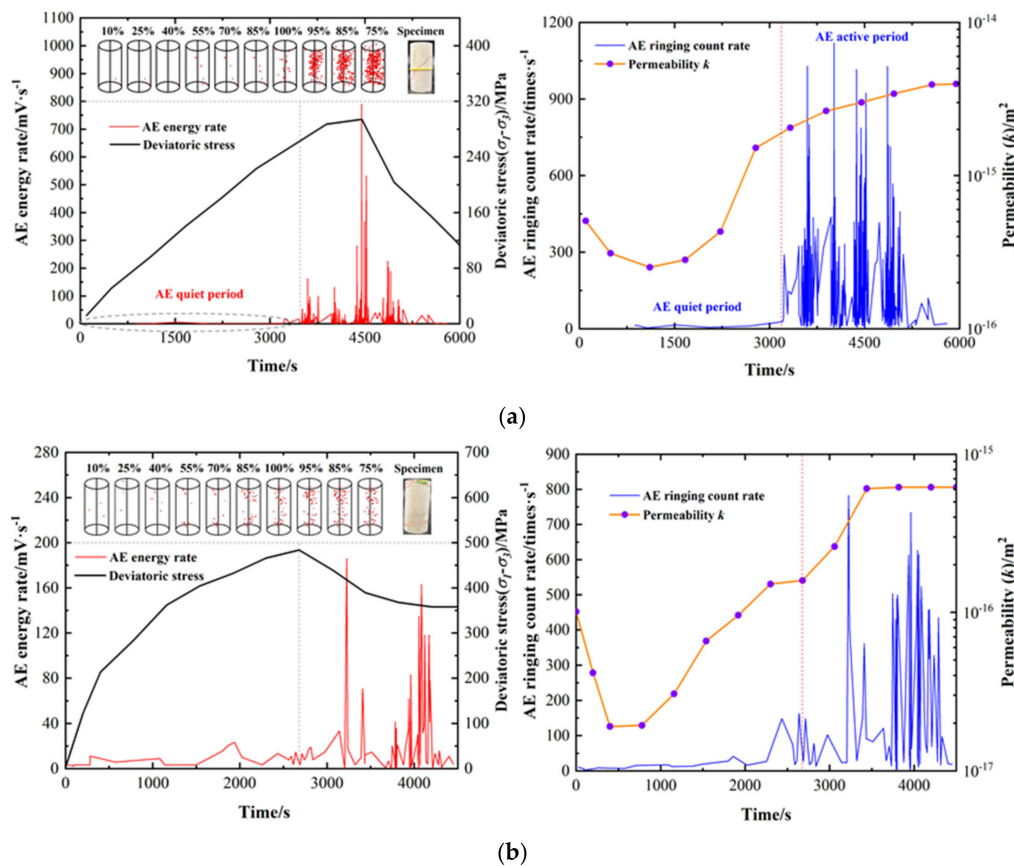


Figure 10. Acoustic emission evolution of dolomite during loading. (a) $\sigma_3 = 15$ MPa; (b) $\sigma_3 = 45$ MPa.

From the perspective of quantitative analysis, the acoustic emission energy rate and ring count rate of dolomite under 15 MPa confining pressure are much larger than those under 45 MPa. At the same time, there are more acoustic emission event points and a higher aggregation degree. The maximum energy rates of AE are 791 and 186 mV/s under the confining pressures of 15 and 45 MPa, respectively, and the maximum ringing count rates are 1119 and 782 times/s, which decrease by 76.5% and 30.1%, respectively.

Under high confining pressure, the acoustic emission event point accumulation zone of dolomite has no obvious convergence and presents a zonal distribution, only scattered in the interior of the sample, which also confirms the fact that high confining pressure inhibits dolomite fracture propagation. By limiting the fracture penetration and hindering gas permeation, the high confining pressure suppresses dolomite permeability. Simultaneously, it also shows that high lateral stress can inhibit crack growth more effectively.

4. Conclusions

- (1) The relationship between the permeability and hydrostatic confining pressure of dolomite is an exponential function, and that between porosity and hydrostatic confining pressure is a power

- function. The functional relationship is obtained by experimental fitting; the permeability and porosity of dolomite decrease with the increase in hydrostatic confining pressure;
- (2) Within 60 MPa confining pressure, with the increase in confining pressure, dolomite specimens change from brittle deformation failure state to ductile deformation state, and the compressive strength increases gradually, confining pressure strengthens the compressive strength of dolomite. Furthermore, under the same confining pressure, the peak stress of conventional triaxial specimen is 10~30% higher than that of the gas–solid coupling specimen; the higher the confining pressure, the smaller the difference, and the residual stress is also the same, which indicates that the compressive strength of dolomite is weakened by gas permeation;
 - (3) In the gas–solid coupling experiment, with the increase in confining pressure, the maximum permeability in the whole loading process gradually decreases. The maximum permeability under confining pressure of 15 MPa is $3.96 \times 10^{-15} \text{ m}^2$, while the maximum permeability under confining pressure of 30, 45, and 60 MPa is reduced to 2.29×10^{-15} , 0.618×10^{-15} , and $0.083 \times 10^{-15} \text{ m}^2$, respectively. This means that high confining pressure will inhibit the permeability of dolomite under critical confining pressure, which is consistent with the law obtained under hydrostatic confining pressure;
 - (4) The higher the confining pressure is, the later the active period of AE occurs, as well as the lower AE energy rate and ring count rate. Concurrently, the fewer the AE event points and the lower the aggregation degree. This further shows that high lateral stress can more effectively inhibit the crack propagation and gas seepage of dolomite.

Author Contributions: Conceptualization, J.L.; data curation, D.X. and Y.Z.; formal analysis, Z.W.; funding acquisition, J.L.; investigation, Y.Z.; methodology, D.X.; project administration, J.L.; resources, Z.W.; software, F.X.; supervision, H.L.; validation, L.W.; visualization, C.L.; writing—original draft, D.X.; writing—review and editing, D.X. All authors have read and agreed to the published version of the manuscript.

Funding: This research was funded by [National Natural Science Foundation of China] grant number [51874202] And the APC was funded by [Jianfeng Liu].

Acknowledgments: The authors wish to offer their gratitude and regards to the colleagues who contributed to this work.

Conflicts of Interest: The authors declare no conflict of interest in this paper.

References

1. Zhang, Q.; Liu, J.F.; Wang, L.; Luo, M.; Liu, H.; Xu, H.; Zou, H. Impurity Effects on the Mechanical Properties and Permeability Characteristics of Salt Rock. *Energies* **2020**, *13*, 1366. [[CrossRef](#)]
2. Ran, L.; Wu, Z.; Han, B. Utilization and development of salt caverns in the field of energy underground storage. *Chin. J. Sci. Technol. Rev.* **2013**, *31*, 76–80. [[CrossRef](#)]
3. Liang, G.; Tian, Y.; Pu, H. Discussion on the development of underground gas storage technology in China. *Chin. J. Gas Heat.* **2014**, *34*, 1–6. [[CrossRef](#)]
4. Dreyer, W.E. *The Science of Rock Mechanics*; Trans Tech Publications: Zurich, Switzerland, 1972.
5. Dreyer, W.E. Results of Recent Studies on the Stability of Crude Oil and Gas Storage in Salt Caverns. In Proceedings of the Fourth International Symposium on Molten Salts, Houston, TX, USA, 3–6 June 1973; pp. 65–92.
6. Ding, G.; Zhang, Y. *Salt Cavern Underground Gas Storage*; Petroleum Industry Press: Beijing, China, 2010.
7. Bennion, B.; Bachu, S. Drainage and imbibition relative permeability relationships for supercritical CO₂/brine and H₂S/brine systems in intergranular sandstone, carbonate, shale, and anhydrite rocks. *SPE Reserv. Eval. Eng.* **2008**, *11*, 487–496. [[CrossRef](#)]
8. Baud, P.; Schubnel, A.; Wong, T.F. Dilatancy, compaction, and failure mode in Solnhofen limestone. *Int. J. Geophys. Res.* **2000**, *105*, 19289–19303. [[CrossRef](#)]
9. Gou, Y.; Wu, Z.; Qi, H. Assessment on the cap rock tightness of the gas storehouse of Anning salt cavern. *J. China Well Rock Salt* **2013**, *44*, 16–19.

10. Zhuo, Q.; Zhao, M.; Li, Y. Dynamic sealing evolution and hydrocarbon accumulation of evaporite cap rocks: An example from Kuqa foreland basin thrust belt. *Chin. J. Pet.* **2014**, *35*, 847–856. [[CrossRef](#)]
11. Chen, W.; Luo, P.; Shan, Y. Analysis of dolomite reservoir characteristics of Xiaoerbulak formation in sugetebulake area, Tarim Basin. *Chin. J. Pet. Geol. Eng.* **2010**, *24*, 12–15.
12. Jiang, L.; Yu, D. Research on reservoir characteristics of Carboniferous Bioclast limestone member in Maigaiti Slope, Tarim Basin. *Chin. J. Peking Univ.* **2003**, *39*, 428–434. [[CrossRef](#)]
13. Li, S.; Zhou, Y. Rock mechanic experiment study of evaluation on cap rock effectiveness. *Chin. J. Pet. Geol. Exp.* **2013**, *35*, 574–578. [[CrossRef](#)]
14. Tillerson, J.R. *Geomechanics Investigations of SPR Crude Oil Storage Caverns*; Sandia Labs: Albuquerque, NM, USA, 1979.
15. Hansen, F.D.; Mellegard, K.D.; Sensen, P.E. Elasticity and Strength of Ten Natural Rock Salt. In Proceedings of the First Conference on the Mechanical Behavior of Salt, State College, PA, USA, 9–11 November 1981; pp. 71–83.
16. Hunsche, U. Fracture Experiments on Cubic Rock Salt Samples. In Proceedings of the First Conference on the Mechanical Behavior of Salt, State College, PA, USA, 9–11 November 1981; pp. 169–179.
17. Hunsche, U.; Albrecht, H. Results of true triaxial strength tests on rock salt. *Eng. Fract. Mech.* **1990**, *35*, 867–877. [[CrossRef](#)]
18. Ni, X. Characteristics and main controlling factors of the Cambrian pre-salt dolomite reservoirs in Tazhong Block, Tarim Basin. *Int. J. Oil Gas Geol.* **2017**, *38*, 489–498.
19. Shao, L.; Han, J.; Ma, F. Characteristics of the Cambrian dolomite reservoirs and their facies-controlling in eastern Tarim Basin. *Acta Sedimentol. Sinica* **2010**, *28*, 953–961.
20. Cuevas, C.D.L. Pore structure characterization in rock salt. *Eng. Geol.* **1997**, *47*, 17–30. [[CrossRef](#)]
21. Peach, C.J. Influence of deformation on the fluid transport properties of salt rocks. *Geol. Ultraiectina* **1998**, *27*, 238–245.
22. Tutolo, B.M.; Luhmann, A.J.; Kong, X.-Z.; Saar, M.O.; Seyfried, W.E. Experimental Observation of Permeability Changes in Dolomite at CO₂ Sequestration Conditions. *Environ. Sci. Technol.* **2014**, *48*, 48. [[CrossRef](#)]
23. Jiang, C.; Duan, M.; Yin, G.; Wang, J.; Lu, T.; Xu, J.; Zhang, D.; Huang, G. Experimental study on seepage properties, AE characteristics and energy dissipation of coal under tiered cyclic loading. *Eng. Geol.* **2017**, *221*, 114–123. [[CrossRef](#)]
24. Guo, J.; Zou, Y.; Cheng, X. Study on acoustic emission characteristics and permeability variation of coal samples under cyclic loading. *Chin. J. Coal Sci. Technol.* **2018**, *46*, 105–109. [[CrossRef](#)]
25. Butt, S. Development of an apparatus to study the gas permeability and acoustic emission characteristics of an outburst-prone sandstone as a function of stress. *Int. J. Rock Mech. Min. Sci.* **1999**, *36*, 1079–1085. [[CrossRef](#)]
26. Kovari, K.; Tisa, A.; Einstein, H.H.; Franklin, J.A. Suggested methods for determining the strength of rock materials in triaxial compression: Revised version. *Int. J. Rock Mech. Min. Sci.* **1983**, *20*, 285–290. [[CrossRef](#)]
27. Sutherland, H.; Cave, S. Argon gas permeability of new mexico rock salt under hydrostatic compression. *Int. J. Rock Mech. Min. Sci.* **1980**, *17*, 281–288. [[CrossRef](#)]
28. Wladis, D.; Jonsson, P.; Wallroth, T. *Regional Characterization of Hydraulic Properties or Rock Using Well Test Data*; Swedish Nuclear Fuel and Waste Management Co.: Stockholm, Sweden, 1997.
29. Alkan, H. Percolation model for dilatancy-induced permeability of the excavation damaged zone in rock salt. *Int. J. Rock Mech. Min. Sci.* **2009**, *46*, 716–724. [[CrossRef](#)]

Publisher’s Note: MDPI stays neutral with regard to jurisdictional claims in published maps and institutional affiliations.



© 2020 by the authors. Licensee MDPI, Basel, Switzerland. This article is an open access article distributed under the terms and conditions of the Creative Commons Attribution (CC BY) license (<http://creativecommons.org/licenses/by/4.0/>).